Research Square

Preprints are preliminary reports that have not undergone peer review.
They should not be considered conclusive, used to inform clinical practice,
or referenced by the media as validated information.

Experimental study on the hierarchical fractal micro-grooved flat-plate loop heat pipe based on Fourier spectrum analysis

Weinan Li
Guangdong University of Technology
Jing Li
Guangdong University of Technology
Jinxia Wu
Guangdong University of Technology
Xin Guo
Guangdong University of Technology
Hui Cheng
Guangdong University of Technology
Jiaming Xie
Guangdong University of Technology
Xingxing Zhang
Dalarna University
Zhangyuan Wang
zwang@gdut.edu.cn

Guangdong University of Technology

Research Article

Keywords: Flat plate loop heat pipe, visualization experiment, two-phase flow characteristics, heat transfer performance

Posted Date: November 26th, 2026

DOI: https://doi.org/10.21203/rs.3.rs-11486945/v1

License: This work is licensed under a Creative Commons Attribution 4.0 International License.
Read Full License

Additional Declarations: No competing interests reported.

Experimental study on the hierarchical fractal micro-grooved flat-plate loop heat pipe based on Fourier spectrum analysis

Weinan Li[a], Jing Li[a], Jinxia Wu[a], Xin Guo[a], Hui Cheng[a], Jiaming Xie[a], Xingxing Zhang[b], Zhangyuan Wang[a,*]

[a]School of Civil and Transportation Engineering, Guangdong University of Technology, Guangzhou, P.R. China, 510006

[b]Department of Energy and Construction Engineering, Dalarna University, Sweden, 79188

Corresponding author: Zhangyuan Wang (Email: zwang@gdut.edu.cn)

Abstract

With the growing popularity of power batteries and the rapid advancement of fast-charging technology, traditional thermal management approaches are struggling to cope with heat dissipation requirements at high power densities. To address this issue, this study developed an innovative flat loop heat pipe featuring a hierarchical fractal micro-grooved channel configuration, and its thermal performance was improved by tuning the combined effects of chamber thickness and filling ratio. A visualization setup was built to capture the dynamic behavior of two-phase flow and the temperature field, which helped clarify the flow-regime transition mechanism and the structural design affecting dynamic heat transfer. The incorporation of primary and secondary micro-grooved channels inside the evaporator increased the heat transfer surface area while offering numerous nucleation sites and rapid vapor escape routes. Using Fourier spectrum analysis, a quantitative approach for classifying operating modes was proposed based on frequency consistency, amplitude level, and phase deviation, which sorted the experimental cases into stable, transitional, and oscillatory categories. The analysis showed that the instability of two-phase flow was linked to the dominant frequency of temperature fluctuations. According to the results, the chamber thickness should be properly matched with the filling ratio and heating

power, and a suitable combination can lower thermal resistance through the combined benefits of vapor-pressure-driven flow and flow-regime optimization. The relationship between chamber thickness and thermal resistance was found to be nonlinear, with the influences of filling ratio and heating power strongly dependent on the chamber structure. This research offers useful guidance for designing efficient and reliable thermal management systems for high-power electronics and electric vehicle batteries.

Keywords: Flat plate loop heat pipe, visualization experiment, two-phase flow characteristics, heat transfer performance

Highlights

- A novel hierarchical fractal micro-grooved flat-plate loop heat pipe was proposed and experimentally validated.
- A visualization platform was constructed to reveal the dynamic evolution of two-phase flow and temperature field under varying chamber thicknesses, filling ratios, and heating powers.
- A Fourier spectrum-based quantitative classification method was developed to identify stable, transitional, and oscillatory operating modes and to correlate two-phase flow instability with the dominant frequency of temperature fluctuations.
- An optimization strategy was proposed, demonstrating that dynamic matching among chamber thickness, filling ratio, and heating power reduced thermal resistance.

Nomenclature

D	Dimension of similarity
F_a	Average frequency (Hz)
F_c	Condenser frequency (Hz)
F_e	Evaporator frequency (Hz)

FR	Filling ratio (%)
F_Q	Nyquist frequency (Hz)
f_s	Sampling frequency (Hz)
N	Number of the secondary micro-grooved channels
Q	Heating power (W)
r	Scaling ratio of the secondary to the primary micro-grooved channels
R	Total thermal resistance (K/W)
s(f)	Power spectral density of temperature signal
t	Time(s)
T	Temperature (K)
T_i	Average temperature of the i^{th} thermocouple measurement point during stable operation (^oC)
T_t	End time (s)
V	Volume (L)
W_1	Width of the primary micro-grooved channels (mm)
W_2	Width of the secondary micro-grooved channels (mm)

Greek symbols

Δφ	Phase deviation (^{o})
δ	Chamber thickness (mm)
$\Phi_{pp}(\tau)$	Cross-correlation function
τ	Lag time (s)

Subscripts

c	Condenser
e	Evaporator
f	Working fluid
i	Inlet
o	Outlet

Abbreviations

BTMSs	Battery thermal management systems
FFT	Fast Fourier Transform

FLHP	Flat loop heat pipe
FHP	Flat heat pipe
HFMFLHP	Hierarchical fractal micro-grooved flat-plate loop heat pipe
LHP	Loop heat pipe
PCM	Phase change material
PSD	Power Spectral Density

1. Introduction

With the global transition in energy systems, vehicle electrification has accelerated remarkably. According to the report from the International Energy Agency, global electric vehicle sales exceeded 10 million units in 2022, achieving the market penetration rate of 14%, of which the share will be projected to reach 60% by 2030 [1]. According to the industry statistics, China has become the world's largest producer and consumer market for new-energy vehicles. Behind this rapid industrial growth, thermal management of the new-energy-vehicle batteries has gradually emerged as a critical technological bottleneck affecting the driving safety of the vehicles [2,3]. For example, the thermal management of the battery systems must dissipate the heat generated from the operation of the batteries effectively to prevent overheating, resulting in a reduced battery life cycle and even thermal runaway [4,5]. Therefore, the development of effective battery's thermal management systems (BTMSs) is essential for promoting efficient battery operation and extending service life.

The existing BTMSs have employed air cooling [6], liquid cooling [7], phase change material (PCM) cooling[8], and heat pipe cooling technologies [9]. However, important challenges of the above-mentioned BTMSs, e.g., air cooling, liquid cooling and PCM cooling, remain, including excessive operating energy consumption, insufficient adaptability to wide ambient-temperature ranges, and difficulty in maintaining stable operation within the optimal temperature range [10,11]. Heat pipe cooling has demonstrated unique advantages in the thermal management of

new-energy vehicle batteries owing to the ability to operate under harsh conditions, high thermal conductivity, high efficiency, and compact structure [12]. However, during the operation of the conventional heat pipes, the entrainment effect induced by the counter-current flow of the vapor and liquid phases has resulted in a significant increase in flow resistance and deterioration of heat transport performance, severely constraining the system's heat transfer limit.

To overcome the performance limitations of the conventional heat pipes, loop heat pipe (LHP) technology has been developed in the academic community of the high-heat-flux electronic devices, e.g., high-performance batteries [13,14], due to its low vapor entrainment resistance, long-distance multi-directional heat transfer capability, and excellent temperature uniformity, which differ significantly in terms of operating principles, heat transfer capability, and structural adaptability with the conventional heat pipes. A typical LHP consists of the evaporator, reservoir, liquid line, condenser, and vapor line. In recent years, researches have increasingly focused on the following areas, e.g., structural optimization of the evaporator, pipelines, configurations of the multi-evaporators, and improvements in wicks [15-17]. In the field of structural parameter optimization for LHP evaporators, Ling et al. [18] designed the capillary wick structure with 13 vapor channels arranged in parallel within the evaporator. The results showed that the LHP exhibited rapid startup and excellent temperature control capability over the heat load range of 30-180W, maintaining the heat source temperature below 75^{o}C and satisfying the cooling requirements of high-power electronic devices. Structural optimization of LHP lines is a key technical route to overcoming the system heat transfer limits and enhancing its dynamic response characteristics. Tharayil et al. [19] significantly enhanced the system’s performance by optimizing the transport line diameter and filling ratio of the LHP, as shown in Fig. 1. The experimental study revealed that the optimal filling ratio was 30%, yielding the lowest evaporator wall temperature of 94.3^{o}C under the heat load of 380W, with the thermal efficiency ranging from 78% to 87%. Del Col et al. [20] conducted the comparative study on condensation systems with rectangular and

circular channels of identical hydraulic diameter. The experimental results revealed that under high mass fluxes where shear stress was dominant, the difference in heat transfer coefficients between the two cross-sectional geometries becomes negligible. As to the wicks inside the evaporator, extensive researches have been conducted on capillary wick types, wick materials, pore sizes, surface micro-structures, and wettability. Wang et al. [21] developed the spherical-dendritic composite wick structure that effectively reduced thermal conductivity while enhancing liquid transport capability, making it particularly suitable for high-heat-flux scenarios.

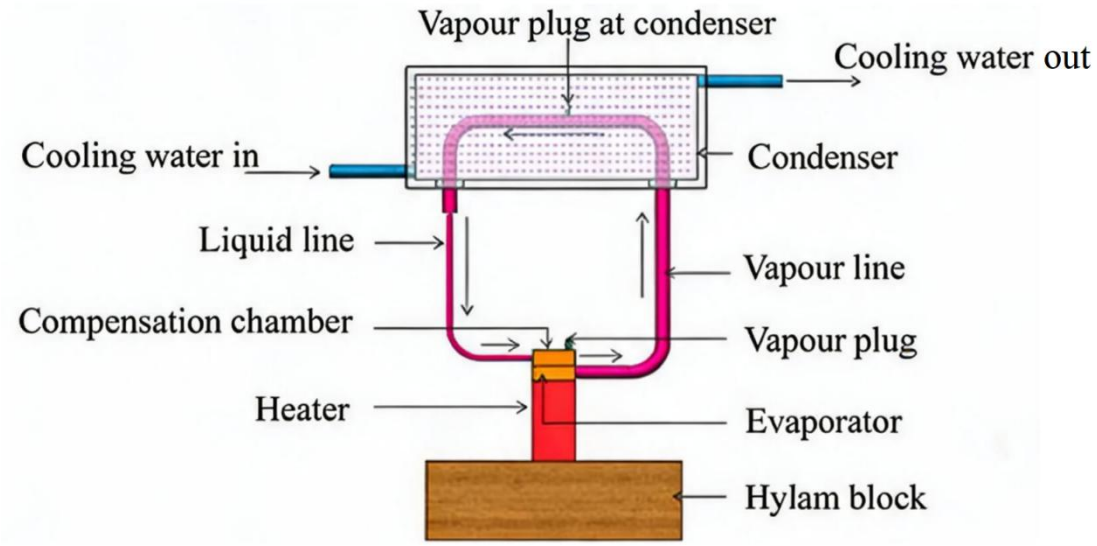


Fig. 1 Pipeline structure design proposed by Tharayil et al. [19]

However, its relatively complex structure and large volume of the LHP limit its application in confined spaces, e.g., limited space of the batteries in the new-energy vehicles [22,23]. In contrast, another unique type of the heat pipe technologies, i.e., flat heat pipe (FHP), with its compact structure and excellent temperature uniformity, is widely used in electronics cooling, yet its limited heat transfer capability makes it difficult to meet the demands of efficient heat dissipation under high heat flux conditions. Combining both the advantages of the LHP and FHP, the flat loop heat pipe (FLHP) emerges as a superior choice, possessing not only the efficient gas-liquid separation characteristics of the LHP, but also the compact structure and temperature

uniformity of the FHP, which enables it to deliver efficient and stable heat transfer performance in confined spaces of the BTMSs [24]. To date, Chernysheva et al. [25] developed the copper-water LHP with the flat elliptical evaporator, as shown in Fig. 2. Studies indicated that, under extreme heat flux conditions (>900W/cm^2), the 3mm heat spreader was capable of reducing the evaporator surface temperature non-uniformity from ±15ºC to within ±3ºC. This structural optimization strategy offered the novel approach for efficient thermal management of miniaturized electronic devices. Tian et al. [26] proposed the miniature LHP featuring the flat evaporator with the eccentric disk configuration, as depicted in Fig. 3. A dual-pore wick, fabricated from sintered nickel powder, was eccentrically mounted within the evaporator cavity to simultaneously form the evaporation and compensation sections. Experimental results demonstrated that the heat pipe exhibited favorable startup characteristics over the heat load range of 2-60W, with the minimum evaporator thermal resistance of only 0.27K/W. Despite its promising potential, the FLHP has faced the following scientific challenges. First, the flat-plate evaporator has induced significant in-plane maldistribution of temperature and vapor quality, yet its coupling with phase-change dynamics and the resulting localized dry-out mechanisms remain unclear. Second, the integration of the compensation chamber with the boiling zone has created complex thermal-hydraulic interactions, for which quantitative design criteria are still lacking. Third, loop-coupled transient oscillations under variable thermal loads have not been systematically characterized, leaving the linkage between operational modes and thermal stability elusive.

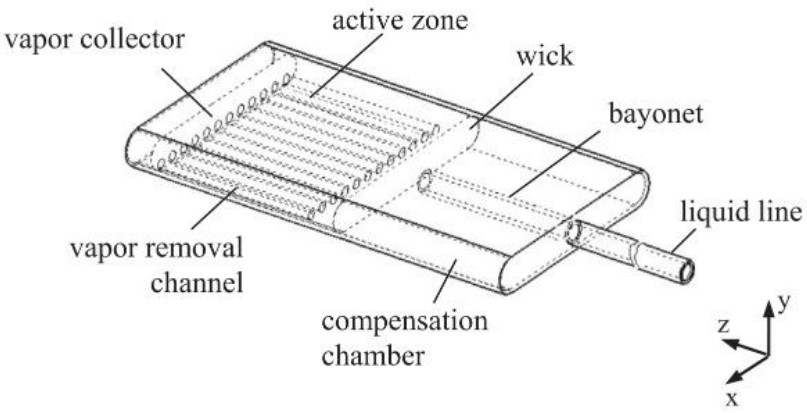


Fig. 2 The copper-water LHP with the flat elliptical evaporator proposed by Chernysheva et al. [25]

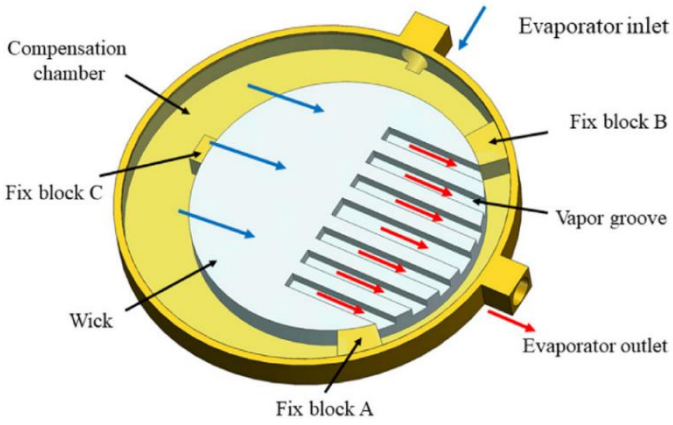


Fig. 3 The miniature LHP with the eccentric disk configuration proposed by Tian et al. [26]

To resolve the above-mentioned challenges faced in the research field of the thermal management for the new-energy vehicle batteries, the hierarchical fractal micro-grooved flat-plate loop heat pipe (HFMFLHP) has been designed and proposed with the structural advantage of the integration of the primary and secondary micro-grooved channels according to the fractal self-similarity rule. This embedded hierarchical fractal structure could increase the specific surface area enhancing the heat exchange efficiency of the evaporator, provide large bubble nucleation regions and high-speed vapor escape channels during boiling of the working fluid, distribute the thermal pressure arising from the temperature differences caused from the high

heat flux of the batteries, and eventually buffer the deformation of the evaporator, which will lead to the favorable heat transfer performance of the specific type of the heat pipe for applications in the BTMSs. In the meantime, to fully understand the internal two-phase flow phenomena existing in the proposed structure, the visualization testing rig has been conducted under different conditions of heating power, filling ratio, and thickness of the chamber in the evaporator. This research has also established the quantitative classification method for operational modes based on Fourier spectrum analysis, investigating the heat transfer performance of HFMFLHP under different operational conditions. This research will be helpful in providing the practical applications of the heat pipes in the new-energy vehicles' BTMSs and widening the market share of the heat pipe globally, and providing the basic theoretical data for the researchers in the relevant fields.

2. Design of the proposed hierarchical fractal micro-grooved flat-plate loop heat pipe (HFMFLHP)

The proposed hierarchical fractal micro-grooved flat-plate loop heat pipe (HFMFLHP) in this research was composed of the evaporator with the primary and secondary micro-grooved channels, linkage pipes between evaporator and condenser (vapor pipe and liquid pipe) and rectangular condenser with the circular counter-flow channel as shown in Fig. 4.

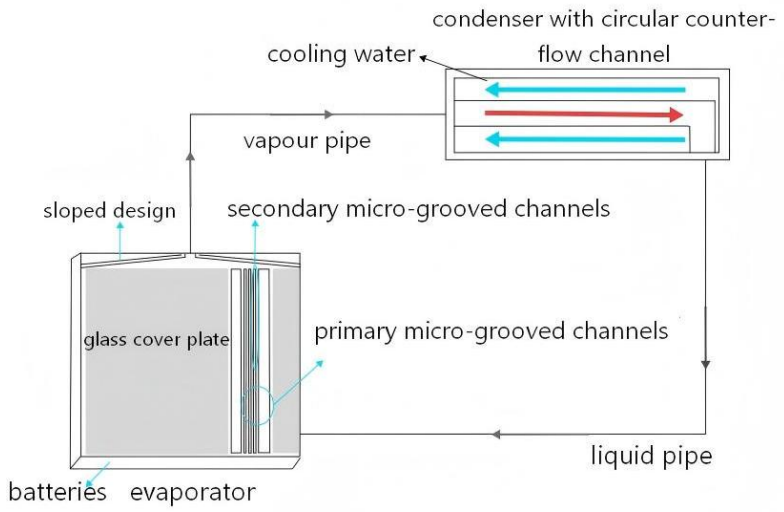


Fig. 4 The schematic of the HFMFLHP

The working principle of the HFMFLHP was that when the heat transferred from the batteries of the new-energy vehicles was absorbed by the evaporator of the HFMFLHP, the working fluid inside, e.g., deionized water, underwent the phase transition from the liquid to the vapor. It should be noted that in order to enhance the heat transfer efficiency, the working fluid underwent the two-dimensional flow. Horizontally, the absorbed heat was transferred to the inner wall of the secondary micro-grooved channels, and then to the primary micro-grooved channels, generating a two-phase mixture of liquid and vapor; while vertically, the generated vapor bubbles would transfer through the inside space of the chamber, and be accumulated in the upper space of the chamber. Then by applying the sloped design underneath the entry of the vapor pipe, the stable and rapid vapor flow would enter the vapor pipe. During the transportation of the working fluid inside the vapor line linking the evaporator and the condenser, the heat losses from the HFMFLHP to the ambient could be negligible since this process could be considered as adiabatic. During the condensation process in the condenser, the heat was released to the cooling water, and the condensed working fluid (composition of the vapor and liquid phase) eventually returned to the evaporator through the adiabatic liquid line under the gravity effect, thereby completing the heat transfer cycle.

Based on the fractal theory, the hierarchical fractal micro-grooved evaporator was composed of 19 parallel primary micro-grooved channels as shown in Fig. 5, each measuring 94mm*3.5mm*1mm (length*width*height). Inside the 19 primary micro-grooved channels, the secondary self-similar hierarchical structure, i.e., secondary micro-grooved channels with the size of 0.5mm in width and 0.5mm in depth, with 4 channels, was established in the height direction. Then, according to the Hausdorff dimension formula [27,28] as shown from Eq. (1) to Eq. (2), the dimension of similarity was calculated and determined to be 0.7124.

$$D=\frac{logN}{log(1/r)} \quad (1)$$

$$r=\frac{W_2}{W_1} \quad (2)$$

By choosing the most appropriate dimension of similarity, the hierarchical fractal structure exhibited stable and uniform flow characteristics, which could prevent the occurrence of the 'dry-out' phenomenon caused by inadequate fluid supplementation. In addition, the hierarchical fractal structure could significantly increase the heat transfer area in specific 'dry-out' regions and enhance the cooling capacity for localized hot spots of the batteries of the new-energy vehicles.

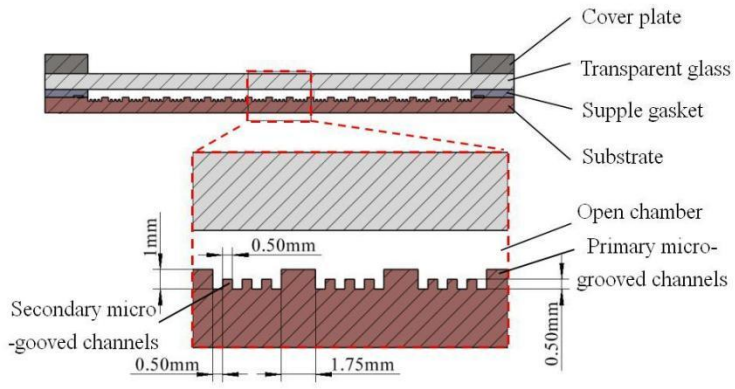


Fig. 5 The cross-section of the evaporator of the hierarchical fractal micro-grooved channels

As to the rectangular condenser with the circular counter-flow channel of the HFMFLHP in Fig. 6, it was designed according to the thermal equilibrium of the working fluid, i.e., deionized water, considering both the heat transfer and flow resistance inside the channels. The length, width and height of the condenser were then determined at 128mm*36mm*7mm with the effective internal size of 98mm*6mm*6mm. In the aspect of the linkage pipes, the sloped design with the tilt angle of 3.3° was adopted at the upper level of the evaporator connecting the entry of the vapor pipe to accumulate the vaporized working fluid and reduce the vapor flow

resistance. The inner and outer diameters of the vapor pipe were 5mm and 6mm with the length of 110mm, and the inner and outer diameters of the liquid pipe were at 3mm and 4mm with the length of 220mm.

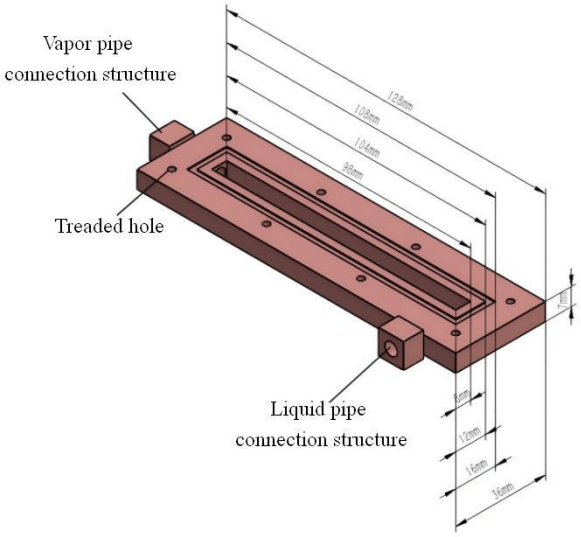


Fig. 6 The schematic of the rectangular condenser with the circular counter-flow channel

The innovations of the proposed HFMFLHP applied in the batteries' thermal management system of the new-energy vehicle lie in the three following aspects. (1) The primary and secondary micro-grooved channels are integrated within the evaporator following the fractal self-similarity rule, which enlarges the surface area, supplies abundant bubble nucleation sites and high-speed vapor escape pathways, redistributes thermally induced pressure, and buffers evaporator deformation; (2) The visualization testing rig is established to characterize the internal two-phase flow behavior under varying heating power, filling ratio, and evaporator chamber thickness; and (3) The Fourier spectrum-based quantitative classification method is developed to identify the operational modes and correlate them with heat transfer performance of the HFMFLHP.

3. Construction of the visualization platform for the HFMFLHP

In order to investigate the two-phase flow characteristics inside the evaporator under different working conditions, the visualization testing rig as shown in Fig. 7 has been designed and established by using the 5mm-thick, high-temperature-resistant, and transparent borosilicate glass cover plate, which can withstand the temperature up to 550°C. The size of the glass cover plate over the evaporator fully matched the size of the evaporator.

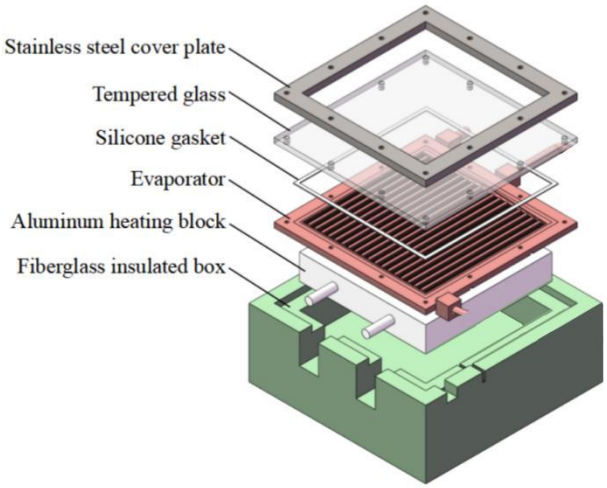


Fig. 7 Schematic of the visualization testing rig

As to the evaporator, the square-shaped stainless steel cover plate with the side length of outer 120mm and inner 98mm and the thickness of 5mm was used to secure and compress the tempered glass cover plate, taking advantage of the stainless steel's capability of high rigidity to prevent the stress-induced deformation of the glass cover plate. In the meantime, the square-shaped silicone gasket with the outer side length of 105mm, inner side length of 100mm, and thickness of 0.1mm was placed between the tempered glass cover plate and evaporator to ensure the air-tightness of the HFMFLHP. Then, the threaded fastener and silicone filling were applied to ensure the tight connection among the stainless steel cover plate, glass cover plate, and evaporator. To minimize the environmental interference to the HFMFLHP, the fiberglass insulated box as the back plate measuring 140mm*140mm*54mm was therefore used to reduce the convective heat losses from the HFMFLHP to the ambient. Besides, the aluminum heating block served as the battery of the new-energy

vehicles, which can be adjusted according to the input voltage and connected to the evaporator using the thermal grease (GK-880).

4. Construction of the testing rig of the proposed hierarchical fractal micro-grooved flat-plate loop heat pipe (HFMFLHP) system

As shown in Fig. 8, the testing rig consisted of the heating system, HFMFLHP system, cooling system, and data acquisition system.

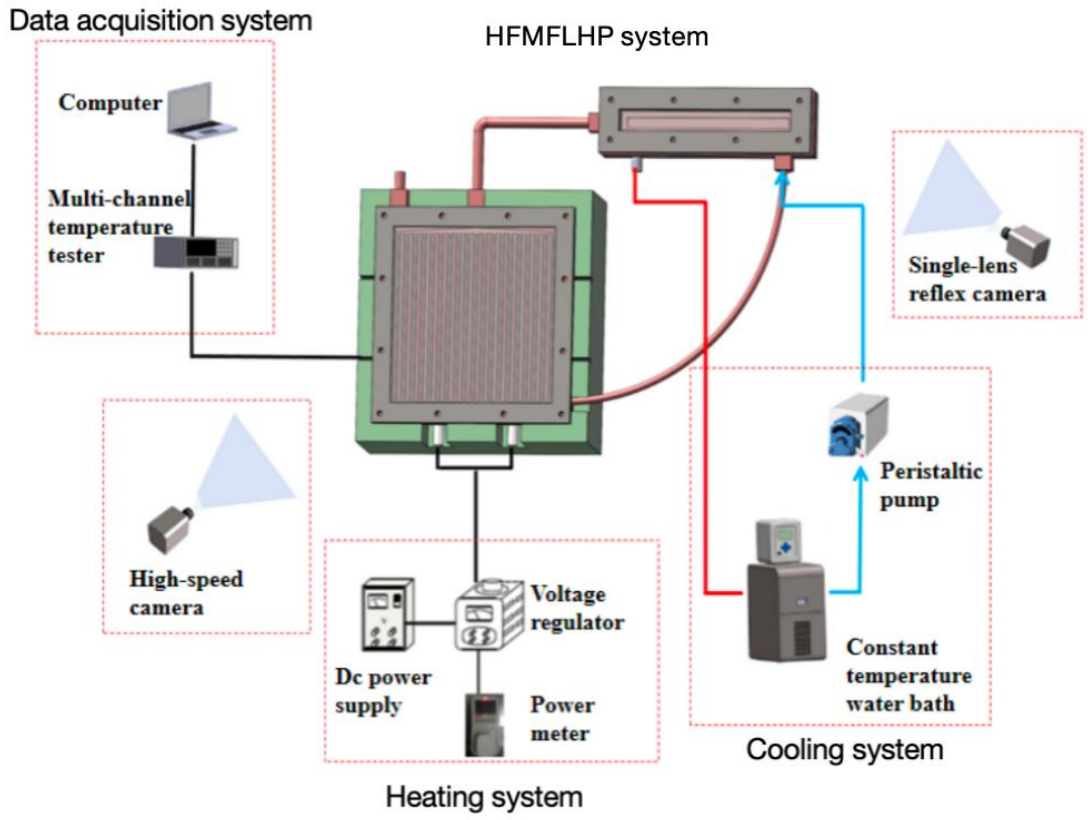


Fig. 8 Construction of the testing rig

The heating system primarily comprised the heating block with the effective heating area of 40mm*40mm, voltage regulator, and dynamometer, with the accuracy of ±0.1W for the overall system. The HFMFLHP system was installed at the inclination angle of 0° (horizontal), and both the vapor and liquid pipes were insulated with thermal insulation cotton (thickness of 5mm). The constant-temperature water bath supplied cooling water at 20°C±0.2°C to the condenser at the flow rate of 4L/min,

with the volumetric flow rate regulated and measured using the float flow-meter (LZB-3WB). Data acquisition was performed using the Agilent Keysight DAQ970A multi-channel temperature tester at the sampling interval of 2s. To reduce the experimental uncertainty and record the surface temperatures of the HFMFLHP, 10 T-type thermocouples (±0.5°C) were deployed at each measurement point in Fig. 9.

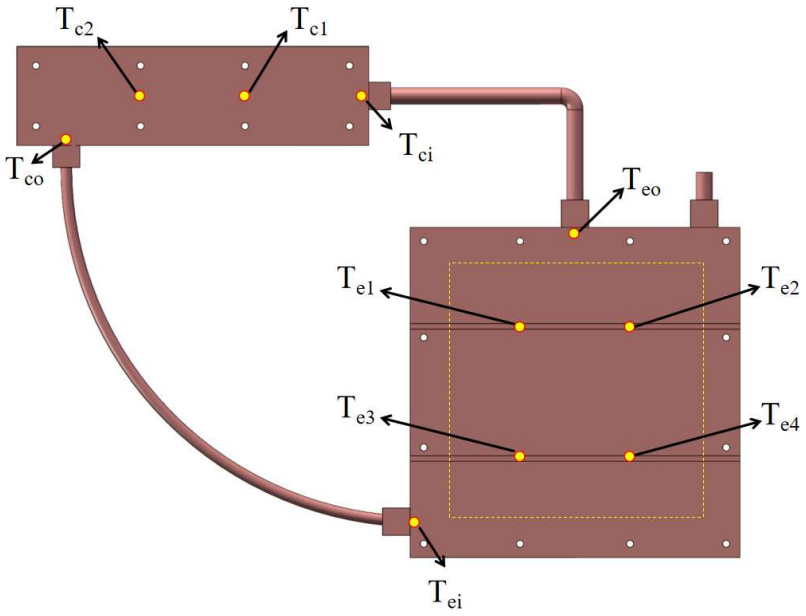
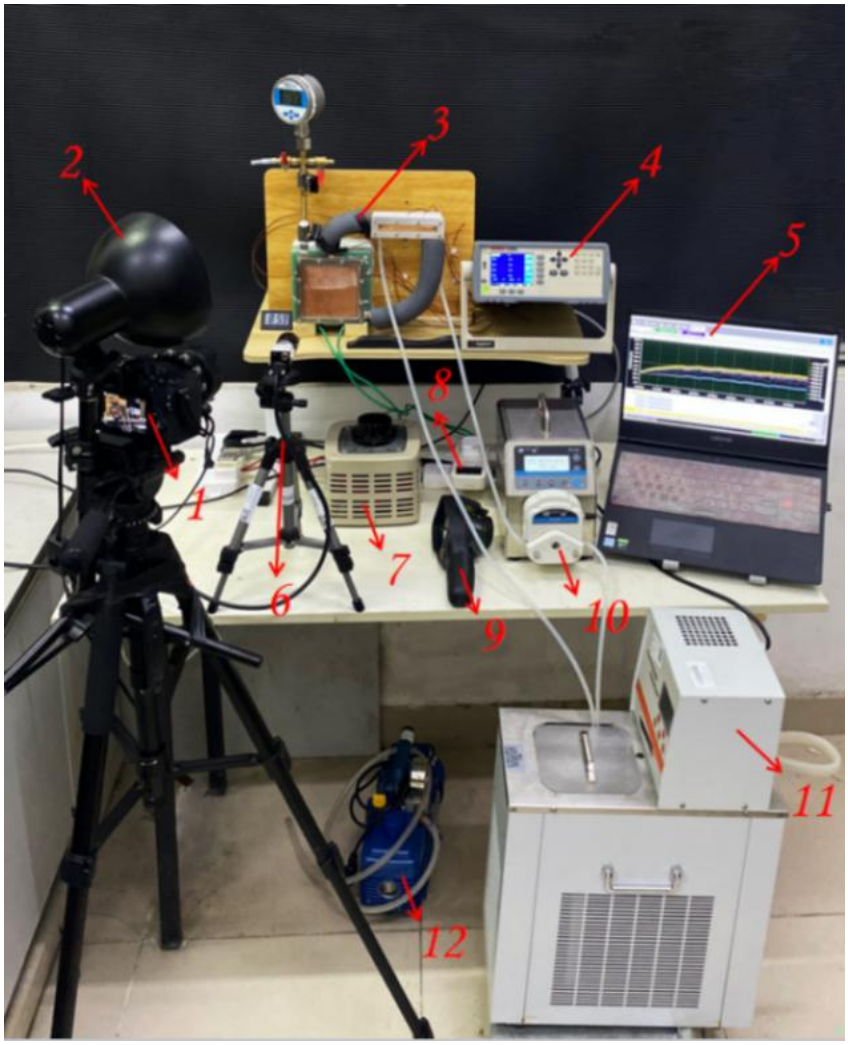


Fig. 9 Location of the T-type thermocouple measurement points

As to the determination of the working conditions, three parameters influencing the operation of the HFMFLHP were considered, i.e., heating power, filling ratio of the working fluid and evaporator chamber thickness, ensuring that the experimental conditions closely resembled the practical electronic cooling scenarios. The input heating power (Q) ranged from 30W to 70W, in increments of 10W. The filling ratio (FR) of the working fluid was defined as the volume of the working fluid charged into the HFMFLHP divided by the total internal volume of the HFMFLHP (including the evaporator, condenser, and vapor/liquid pipes) as in Eq. (3) [29]. Filling ratios of 30%, 50%, and 70% were selected to cover low, medium, and high filling conditions. As to the evaporator chamber thickness (δ), a range of 0-3mm was considered to represent different evaporator chamber heights.

$$FR=\frac{V_f}{V} \quad (3)$$

After connecting all the testing equipment, the experimental photo was shown in Fig. 10. The preliminary experiment comprised three steps. First, the airtightness of the loop heat pipe was tested, after the evaporator, condenser, and vapor/liquid pipes were connected, the vacuum pump (No. 12 in Figure 10) was connected by a flexible hose to the hose barb on the right side of the vacuum gauge. The vacuum pump was then started, and its corresponding valve was closed. After the apparatus had stood for 2 h, the pressure gauge showed no appreciable change, indicating that the apparatus was adequately airtight. Second, the working fluid was charged, after the airtightness test, the right valve was closed, and the left valve, which was connected to a syringe containing the working fluid, was opened. The negative pressure in the evaporator drew all the liquid into it. The filling ratio was set to 50% for the preliminary experiment. The left and lower valves were then closed, completing the evacuation and charging of the loop heat pipe. Third, the heating platform, temperature data acquisition platform, and circulating cooling-water system were switched on to monitor the fluid state in the heat pipe and the temperature fluctuations. To verify the temperature measurements, readings from the infrared thermal image were compared with those from the temperature monitoring platform. Once the heat pipe had operated stably for 30 min and the temperature readings had become nearly stable, the preliminary experiment was terminated.



1-Single-lens reflex camera, 2-fill light, 3-HFMFLHP, 4-multi-channel temperature tester, 5-Computer, 6-high-speed camera, 7-voltage regulator, 8-power meter, 9-infrared detector, 10-peristaltic pump, 11-constant temperature water bath, 12-vacuum pump

Fig. 10 The experimental photo

5. Classification of the operating mode of the HFMFLHP using Fourier spectrum analysis method

In order to systematically investigate the heat transfer characteristics of the HFMFLHP during its operation stage, three operating modes of the proposed HFMFLHP, i.e., stable, transitional and oscillatory, have been classified by extracting

the spectral features of temperature fluctuations (i.e., frequency consistency, amplitude, and phase deviation) through Fourier spectrum analysis.

5.1 Definition of the Fourier spectrum analysis

In this research, for the temperature fluctuation data during the operation stage of the HFMFLHP, the Power Spectral Density (PSD) curve of the temperature signal can be obtained by using the Fast Fourier Transform (FFT) algorithm, and the characteristic frequency of the time-variation of the temperature can then be identified through spectral feature extraction techniques. The detailed calculation process was as follows.

Firstly, the time-domain temperature data during the operation were converted by FFT into PSD data in the frequency domain as follows [30]:

$$\emptyset_{pp}(\tau)=\lim_{T_t\to\infty}\frac{1}{T_t}\int_{-T_t/2}^{T_t/2}P(t)(t+\tau)dt \tag{4}$$

$$s(f)=\int_{-\infty}^{\infty}\emptyset_{pp}(\tau)e^{-j2\pi f\tau}d\tau \tag{5}$$

Meanwhile, to recover all Fourier components of the periodic signal and perform error-free sampling, the Nyquist frequency was used as the sampling rate [30]:

$$F_Q=\frac{f_s}{2} \tag{6}$$

In this study, the sampling period was taken as 2s, corresponding to the sampling frequency of 0.5Hz. Then, the Nyquist frequency (minimum sampling rate) was thus calculated to be 0.25Hz.

Secondly, the operating modes of the HFMFLHP were divided into stable mode, transitional mode, and oscillatory mode, and the classification was based on three perspectives, i.e., frequency consistency, amplitude level, and phase deviation.

According to the frequency-consistency characteristics, three forms, A, B, and C, were defined. The characteristics of form A were that the temperature fluctuation periods at all measurement points were consistent, indicating that the HFMFLHP system was in a stable state with good synchronization. For form B, the characteristic dominant frequency of the evaporator was inconsistent with those of the other measurement points; this mode indicated the desynchronization between the temperature fluctuation period of the evaporator and those of the other measurement points. As to form C, the characteristic dominant frequency of the condenser was inconsistent with those of the other measurement points. This mode C also indicated the desynchronization between the temperature fluctuation period of the condenser and those of the other measurement points.

For the acquisition of temperature amplitude characteristics, the standard deviation, i.e., the parameter used to characterize the dispersion of an observed data set relative to its mean, was introduced to describe the intensity of temperature fluctuations in the system. In order to clarify the influence of each measurement point on the whole system's dynamic behavior, the weighted average method was used to classify the amplitude according to the amplitude of temperature fluctuations in all experimental data. Then the time-domain temperature data were divided into three categories: steady (amplitude 0-2), moderate (2-5), and large (5-10).

Phase deviation ($\Delta\varphi$) can reflect the time difference between temperature signals and synchronization of fluctuations among different measurement points. The calculation formula was as follows [30]:

$$\Delta\phi=\frac{F_e-F_c}{F_a} \quad (7)$$

Based on the results from the Fourier spectrum analysis, the phase deviation under each operating condition was calculated and classified into the following three categories, i.e., small, moderate and large. Small phase deviation (<30°): The fluctuations between signals were almost synchronous, indicating that the system was relatively stable in terms of temperature fluctuations. Moderate phase deviation (30°-90°): There was a certain lag between signals, suggesting that there may be differences in heat flow or fluid flow among the measurement points of the system. Large phase deviation (>90°): The fluctuations between signals differed considerably, indicating that the system may exhibit significant instability.

5.2 Classification of the operating mode of the HFMFLHP

Then, the time-domain temperatures from the 36 experimental conditions were comprehensively classified into three main modes. The specific criteria and their characteristics were presented as follows:

(1) Stable mode: The frequencies at the measurement points were consistent, the amplitude was steady, and the phase deviation was small; or the frequencies were quasi-continuous, but the amplitude was steady and the phase deviation was small. This indicated that the system was in a stable operating state.

(2) Transitional mode: The frequencies at the measurement points were consistent, the amplitude was moderate, and the phase deviation was small. This indicated that the system exhibited a certain degree of fluctuation but had not yet entered a severe oscillatory state.

(3) Oscillatory mode: The frequencies at the measurement points were quasi-discontinuous, and the phase deviation was moderate/large or the amplitude was moderate/large; or the frequencies at the measurement points were inconsistent, and the amplitude was moderate/large or the phase deviation was moderate/large. This indicated that the system exhibited relatively severe instability.

6. Analysis of the visualization experimental results for the HFMFLHP under different operating modes

To more precisely reveal the actual mechanism of the heat transfer performance of the HFMFLHP, the results from the visualization experiments were analyzed based on the classification of the operating modes (i.e., stable mode, transitional mode, and oscillatory mode) of the HFMFLHP under different operating conditions (i.e., filling ratio of working fluid, heating power, and evaporator chamber thickness). It should be noted that due to the limited length of this article, typical cases have been selected from the original 36 cases for analysis.

6.1 Analysis of the visualization experimental results for the HFMFLHP in stable mode

In order to investigate the influence of the operating conditions on the heat transfer performance of the HFMFLHP, the experimental results were analyzed first according to the evaporator chamber thickness δ, and then discussed in terms of filling ratio FR and heating power Q.

Fig. 11 presented the phase-change behavior of the working fluid in the evaporator under the stable mode when δ=0mm. In this figure, the yellow line delineated the maximum wetting region, and the blue line marked the liquid-phase coverage area. From this figure, when δ=0mm, and Q=30W, the liquid-phase area fraction within the evaporator increased significantly with increasing filling ratio, as can be seen by comparing Fig. 11(a) and (b). In the meantime, due to the re-fluxed sub-cooled liquid, the increased liquid-phase coverage area and wetted area in the evaporator enabled the liquid working fluid to be distributed relatively uniformly within the evaporator. This distribution was maintained in dynamic equilibrium, which sustained stable operation via balanced phase-change heat transfer. At δ=0mm and FR=30% (Q=30W), nucleate and thin-film boiling contributions remained comparable, with thin-film vapor generation compensating for the low charge and minimizing temperature fluctuations.

At FR=70% (Q=30W), nucleate boiling dominated the liquid-covered area, while thin-film evaporation acted as an auxiliary mode, forming the dual-mode that maintained stable evaporator operation. Despite their different contribution ratios, both cases satisfied the criterion of dynamic equilibrium between the two heat transfer modes and were thus classified as stable mode.

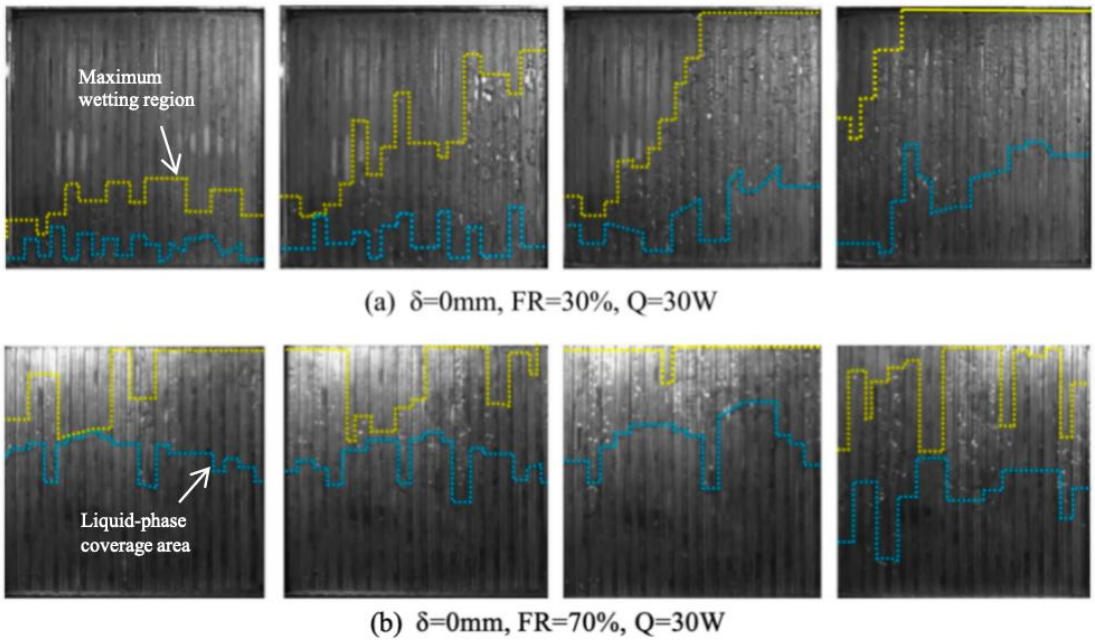


Fig. 11 Visualization image of the evaporator with δ=0mm in stable mode

Fig. 12 showed stable-mode evaporator visualization for δ>0mm. All structures still operated in the stable mode with relatively small gas-liquid interface fluctuations. However, as δ increased, the larger open space allowed bubbles to grow and rupture more freely, making the interface fluctuations more pronounced than in the δ=0mm case, though they remained within the stable range. At δ=1mm, FR=70%, and Q=30W in Fig. 12(a), the liquid-phase fraction exceeded 50% and the wetted area approached 100%, resembling the δ=0mm case in Fig. 11(b) because nucleate boiling dominated the expanded liquid-phase region and combined with thin-film evaporation to ensure dual-mode heat transfer. For other δ>0mm structures (δ=2 and 3mm), the liquid-phase coverage and maximum wetted area also maintained dynamic equilibrium, because

the low power input restricted evaporation and thus caused insufficient vapor driving force, which was compensated by thin-film boiling.

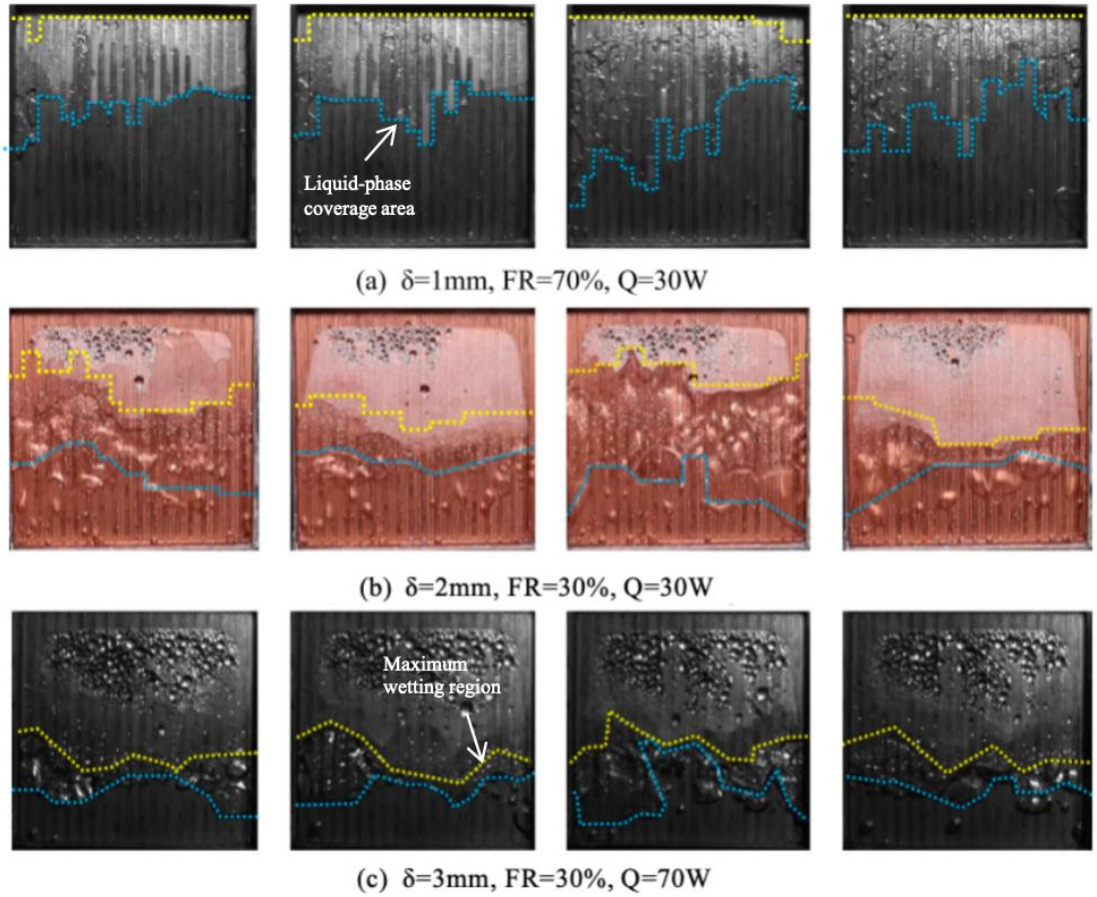


Fig. 12 Visualization image of the evaporator with δ>0mm in stable mode

A comparison between the δ=0mm and δ>0mm structures in Fig. 11 and Fig. 12 revealed that structural differences led to similar phase-change heat transfer modes but distinct dynamic characteristics. At δ=0mm, the confined structure caused relatively large synchronized fluctuations in the wetted and liquid-phase areas; at δ>0mm, the open chamber increased the degrees of freedom of bubble nucleation-detachment, reducing liquid-phase fraction variations but enlarging vapor-liquid interface fluctuations and wetted-region changes. In other words, the fluctuation shifted from synchronized area changes to interface-dominated fluctuations. All structures achieved dynamic equilibrium through the combined action of nucleate and thin-film boiling, though via different pathways, ultimately

forming a synergistic dual-mode heat transfer mechanism. The δ=0mm structure relied on vapor compensation by thin-film boiling in the wetted region, whereas the δ>0mm structure maintained the liquid-phase area through the buffering effect of the chamber, with the expanded interface enhancing thin-film evaporation.

6.2 Analysis of the visualization experimental results for the HFMFLHP in transitional mode

Following the stable-mode analysis, the transitional mode behaviors under δ=0, 1, 2, and 3mm were discussed below to clarify the effect of the operating conditions of the HFMFLHP.

Fig. 13 showed three transitional mode cases at δ=0mm. At FR=30%, Q=50W, the wetted area exceeded the liquid-phase area because thin-film boiling extended the wetted region beyond the liquid-phase coverage and distributed more uniformly than at Q=30W in Fig. 11(a), suggesting that thin-film-boiling-dominated heat transfer with higher power reduced temperature fluctuations. At FR=50%, Q=70W, the wetted area fluctuated more strongly, because the higher evaporation rate was not matched by sufficient condensate return, reducing liquid-phase area and wetting uniformity and increasing temperature fluctuation amplitude. At FR=70%, Q=70W, the larger filling ratio increased the liquid-phase fraction, indicating that filling ratio strongly affected evaporator phase-change heat transfer.

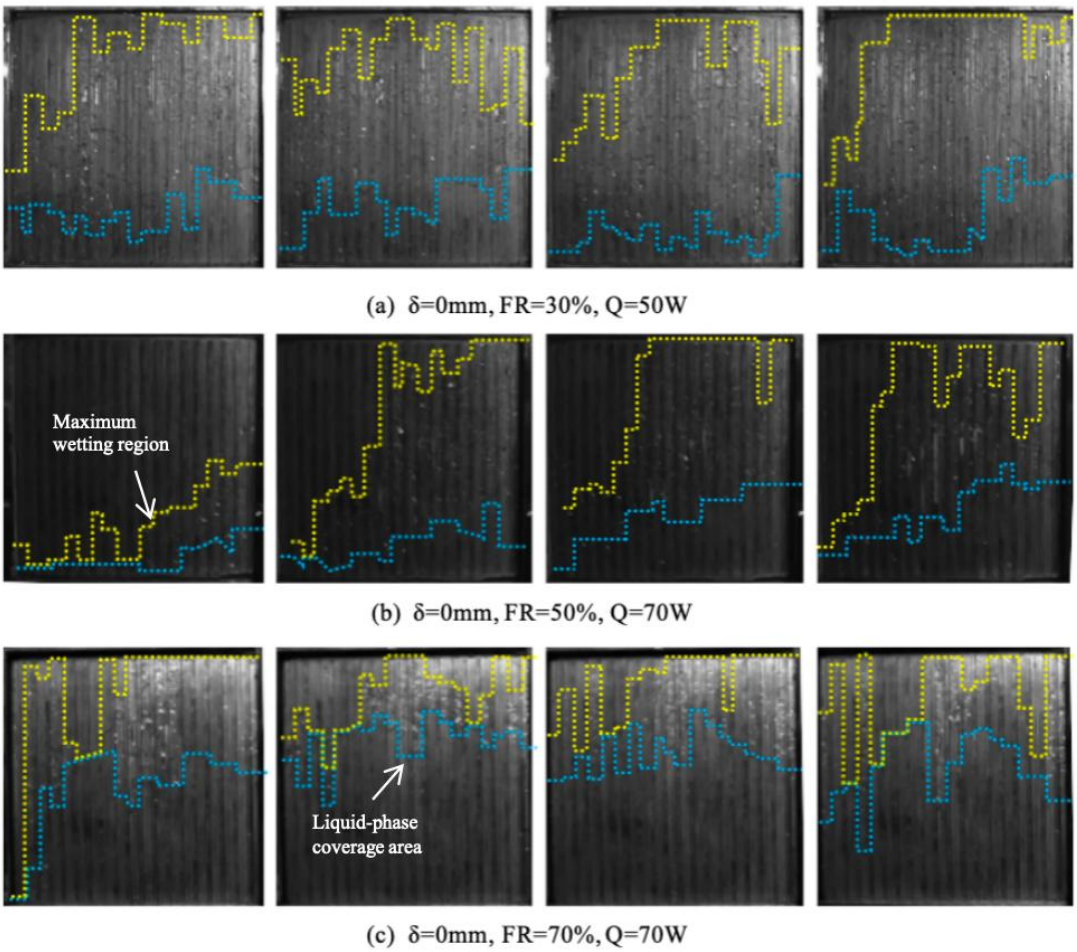


Fig. 13 Visualization image of the evaporator with δ=0mm in transitional mode

Fig. 14 showed three cases at δ=1mm. At FR=30%, Q=30W (Fig. 14(a)), the liquid-phase fraction and wetted area were relatively small because the low heating power reduced the evaporation rate and weakened the driving force, causing moderate temperature fluctuations. At FR=30%, Q=70W (Fig. 14(b)), the wetted area and liquid-phase fraction were larger than at Q=30W in Fig. 14(a), as the higher power enhanced evaporation, strengthened the driving force, and promoted timely liquid return. Despite the larger wetted area and liquid-phase fraction, marked interface fluctuations persisted, so this case remained a transitional mode. At FR=50%, Q=30W, the wetted area fluctuated substantially, reaching 90% of the inner surface. The higher filling ratio caused liquid accumulation, strong sub-cooling, and moderate temperature fluctuations.

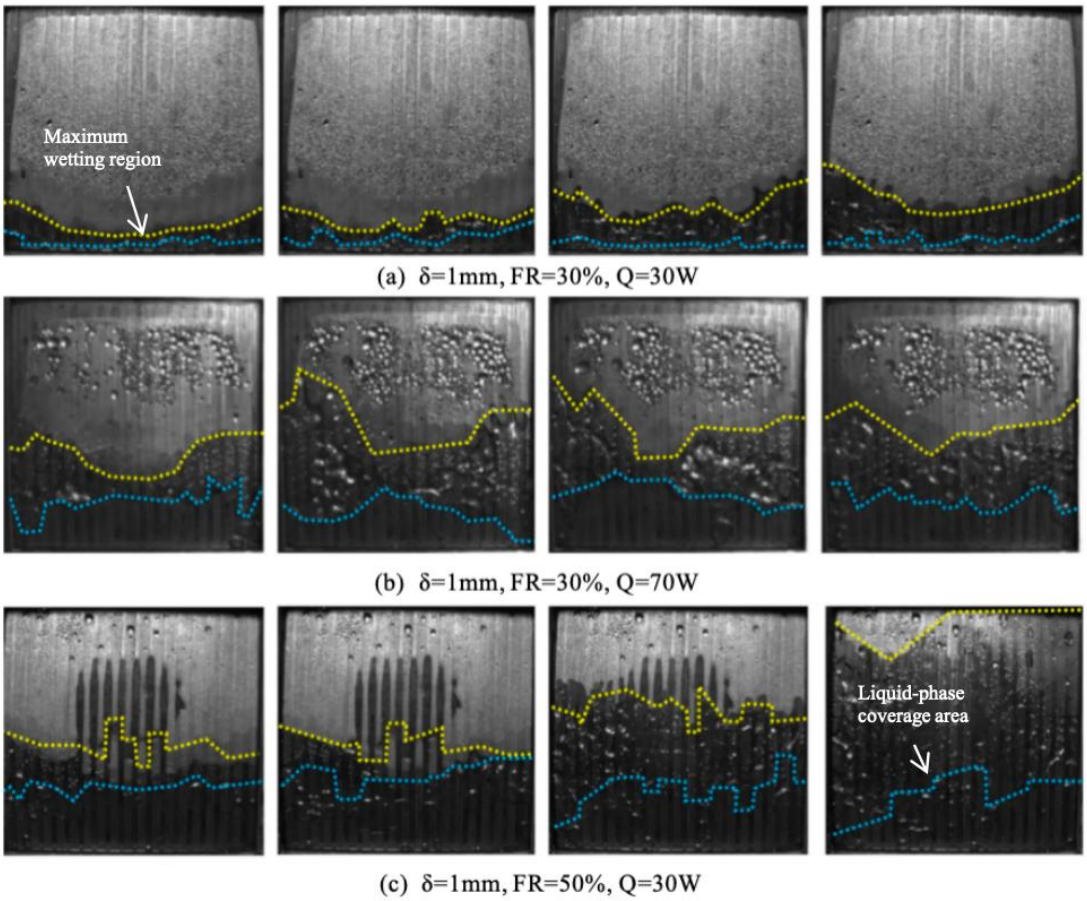


Fig. 14 Visualization image of the evaporator with δ=1mm in transitional mode

Fig. 15(a) showed that at δ=2mm, FR=30%, and Q=50W, vapor-liquid interface, wetted-area, and liquid-phase fluctuations were markedly larger than under stable condition at Q=30W in Fig. 12(b), indicating stronger disturbances and larger temperature fluctuations. Fig. 15(b) showed that at δ=2mm, FR=50%, and Q=50W, liquid-phase and wetted-area fluctuations increased further, with the maximum wetted area exceeding 80% of the evaporator area. This was attributed to the higher filling ratio promoting bubble detachment and breakup during nucleate boiling, causing vigorous boiling with large bubbles and wetted-region oscillation that induced temperature fluctuations at the same heating power.

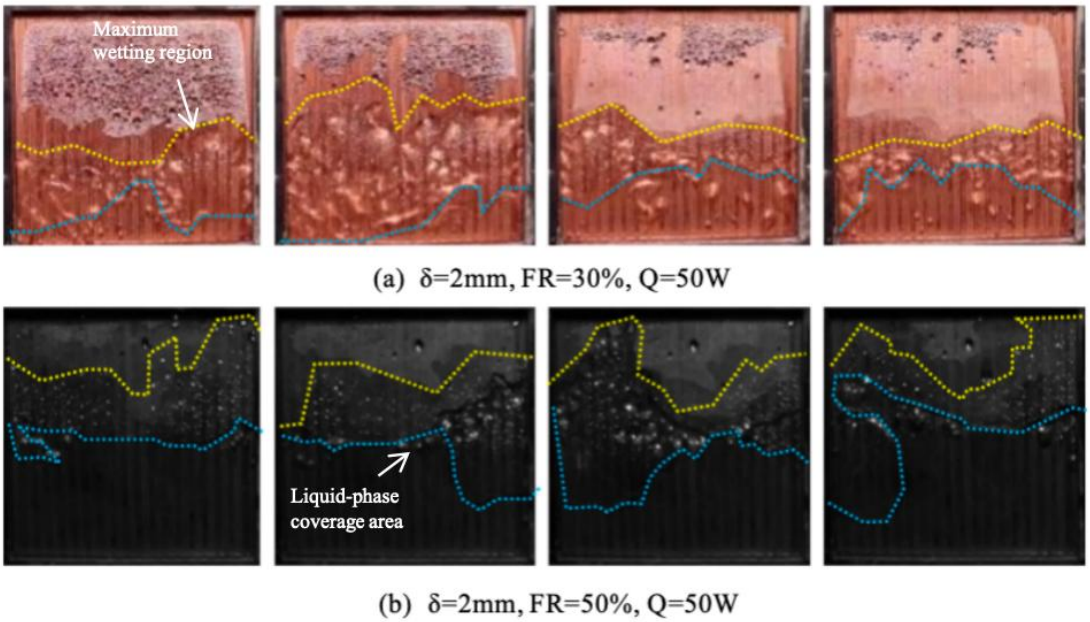


Fig. 15 Visualization image of the evaporator with δ=2mm in transitional mode

For Fig. 16(a) at δ=3mm, FR=30%, and Q=50W, the liquid-phase region fluctuated with numerous nucleation sites, indicating vigorous nucleate boiling and sufficient vapor pressure; the larger structure retained liquid but caused greater interface fluctuations, amplifying temperature fluctuations. The wetted area and liquid-phase fraction changed little versus the stable Q=70W case in Fig. 12(c). As shown in Fig. 16(b) at δ=3mm, FR=50%, Q=70W, the liquid phase occupied 50% of the evaporator area with slight fluctuation, while the wetted area fluctuated considerably, suggesting that higher filling ratio increased temperature fluctuation compared with Fig. 12(c).

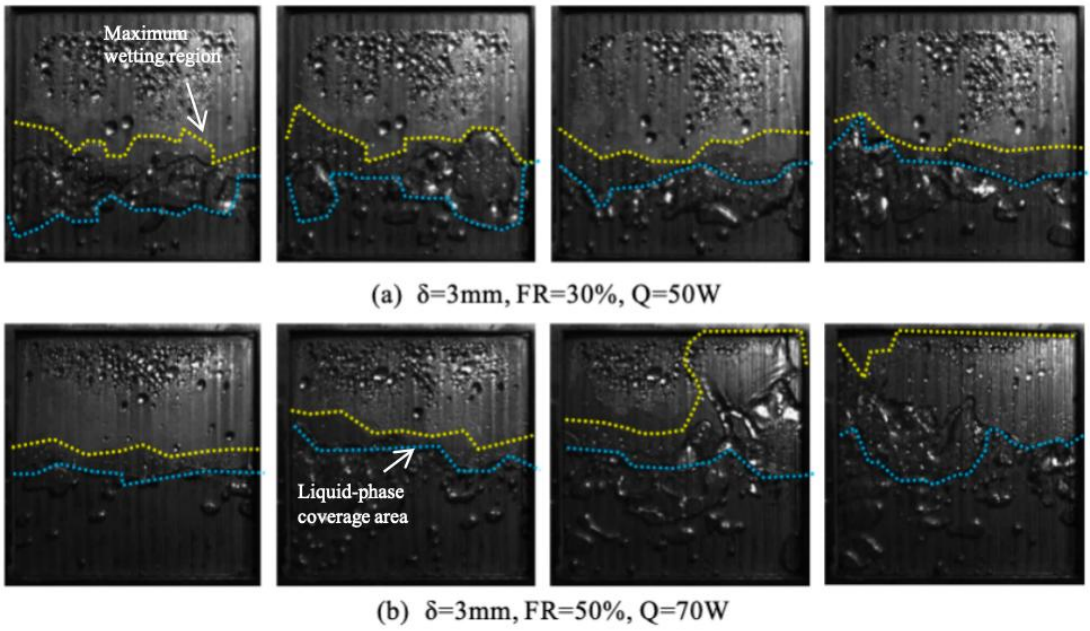


Fig. 16 Visualization image of the evaporator with δ=3mm in transitional mode

6.3 Analysis of the visualization experimental results for the HFMFLHP in oscillatory mode

To clarify how chamber thickness affected the oscillatory-mode behavior of the HFMFLHP, the cases for δ=0-3mm were further examined below.

Fig. 17 showed that the δ=0mm structure exhibited an oscillatory mode at FR=30%, Q=70W and FR=50%, Q=30W, with alternating wetting and dryout in the evaporator. The upper half initially dried out while the lower half remained wetted by capillary action, after which the liquid level rose until the entire evaporator was rewetted. This indicated a nonuniform liquid distribution caused by the filling ratio and heating power. Capillary forces drove liquid upward through the micro-grooved channels, but no stable state was reached, causing repeated wetting and dryout. The nonuniform distribution combined with continuous capillary action was therefore considered a primary cause of the oscillatory mode.

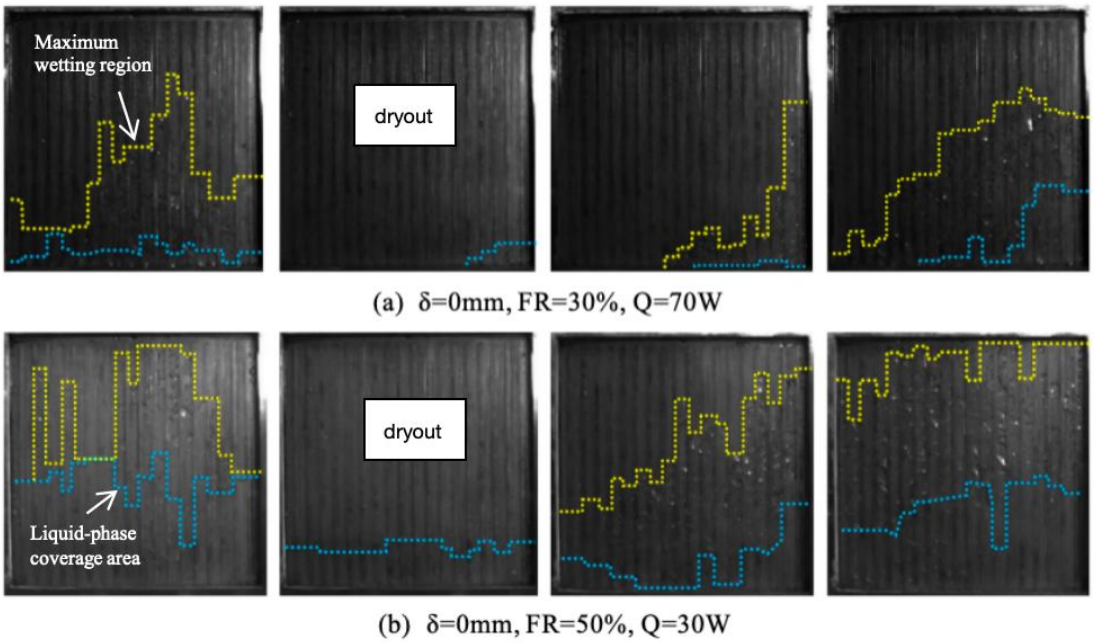


Fig. 17 Visualization image of the evaporator with δ=0mm in oscillatory mode

For the δ=1mm structure, the oscillatory mode occurred at FR=30% and 50% with Q=50W. Fig. 18(a) showed that at FR=30% and Q=50W, the wetted area in the evaporator was smaller than in the transitional mode at δ=1mm, FR=30%, and Q=70W (Fig. 14(b)). The lower heating power weakened thin-film boiling, reducing the evaporation rate and vapor driving force. Under these conditions, return-flow resistance contributed to the temperature fluctuations characteristic of the oscillatory mode. At FR=50% and Q=50W (Fig. 18(b)), disturbances of the working fluid in the evaporator intensified. The combination of lower heating power and greater working-fluid charge reduced the vapor space in the evaporator and restricted vapor diffusion, together producing the large-amplitude temperature fluctuations observed in the oscillatory mode, because the larger liquid charge occupied more of the open chamber while the low power generated insufficient vapor.

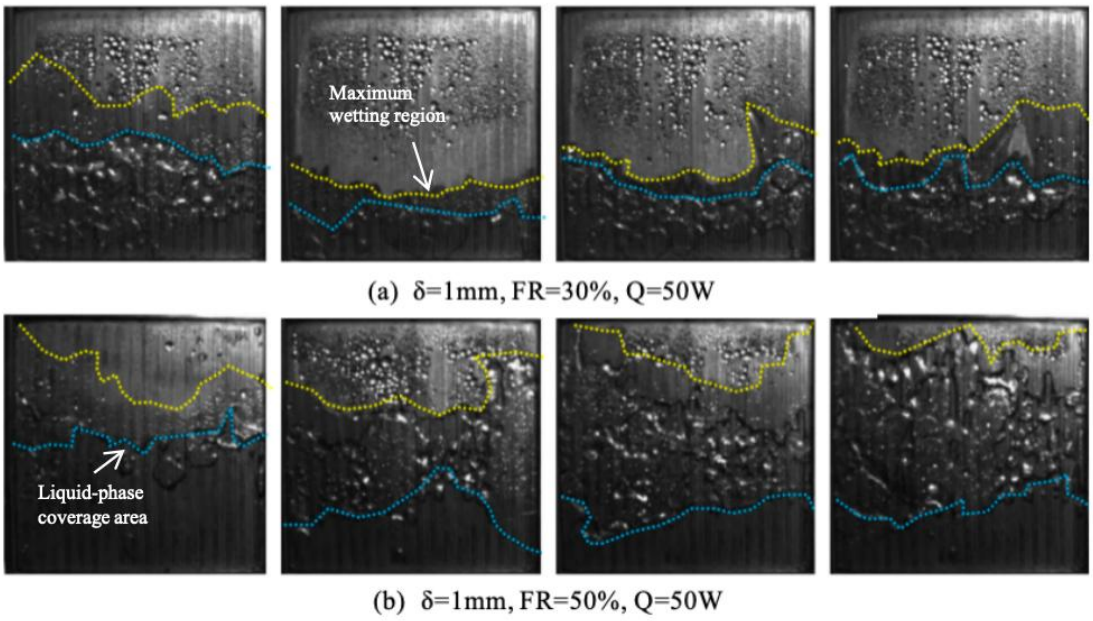


Fig. 18 Visualization image of the evaporator with δ=1mm in oscillatory mode

For the δ=2mm configuration, the oscillatory mode occurred at FR=30% and Q=70W (Fig. 19(a)) because the higher heating power affected the return flow-pattern transition. At FR=50%, and Q=30W, the vapor-liquid interfaces fluctuated substantially in both the transitional mode at Q=50W (Fig. 15(b)) and the oscillatory mode at Q=30W (Fig. 19(b)), indicating that the lower heating power provided insufficient driving force. The return-liquid therefore was abruptly injected into the evaporator, producing the pronounced temperature fluctuations characteristic of the oscillatory mode.

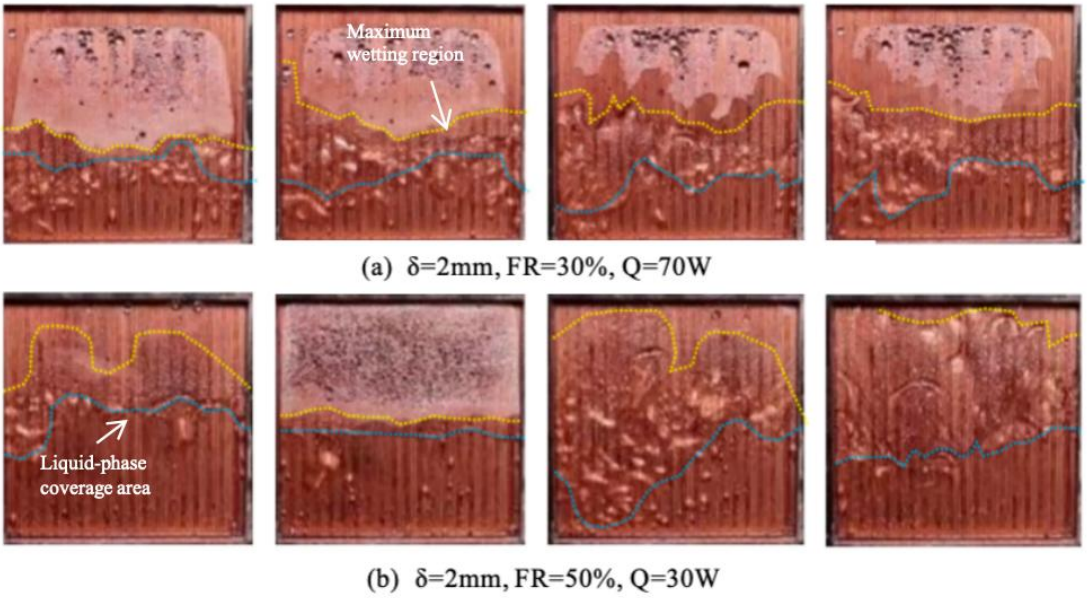
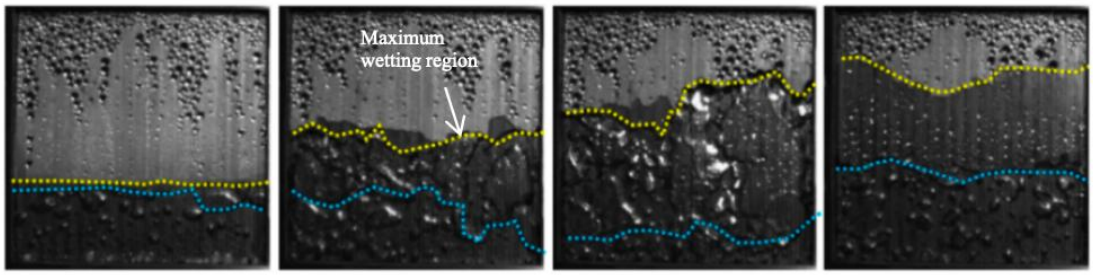
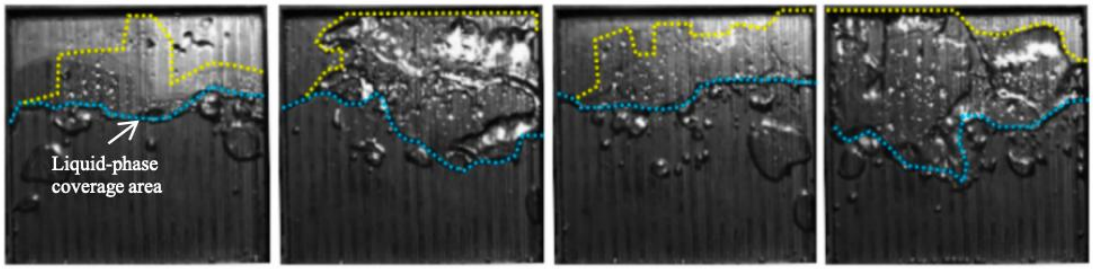


Fig. 19 Visualization image of the evaporator with δ=2mm in oscillatory mode

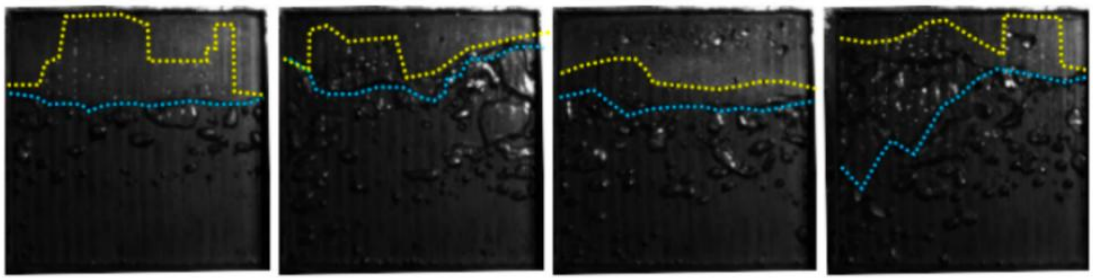
Under oscillatory operation, the δ=3mm open chamber design aggravated the dynamic instability of the vapor-liquid interface as shown in Fig. 20. At FR=30% and Q=30W, the low filling ratio limited liquid-phase coverage, but the open chamber promoted localized intense nucleate boiling, and bubble coalescence and breakup generated periodic vapor-pressure pulsations. At FR=70% and Q=30W, the sufficient filling ratio maintained nucleate boiling as the dominant mode, with the liquid-phase fraction above 80%, but the low power caused a mismatch between vapor-generation rate and chamber volume, and delayed wetted-region restoration induced intermittent temperature fluctuations. At FR=70% and Q=70W, the higher power stabilized the liquid-phase coverage, indicating that the 3mm thickness buffered parameter disturbances by enlarging the phase-change space. The δ=3mm structure maintained the two-phase distribution at high filling ratios, but inter-facial instability prevented dynamic equilibrium, revealing the fundamental limitation of an excessively open chamber design in suppressing oscillatory operation.



(a) δ=3mm, FR=30%, Q=30W



(b) δ=3mm, FR=70%, Q=30W



(c) δ=3mm, FR=70%, Q=70W

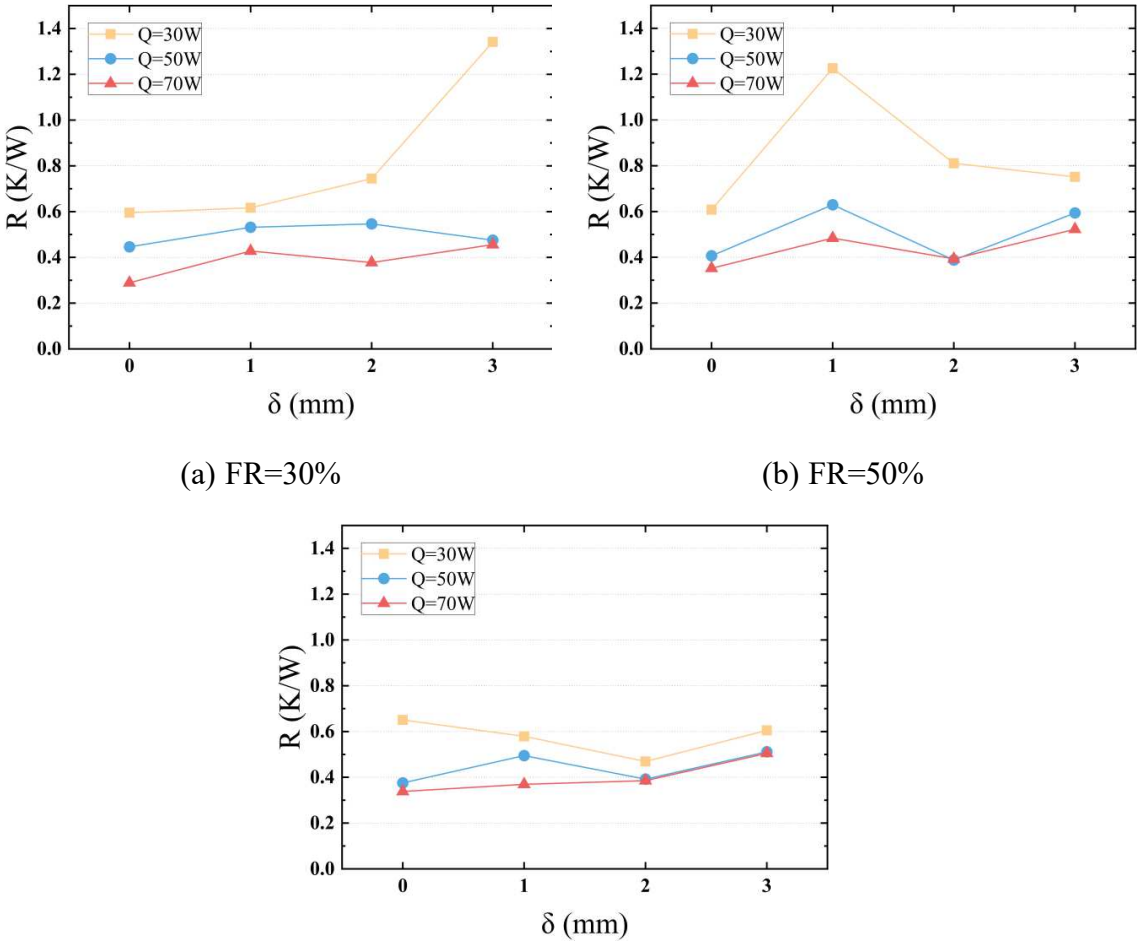
Fig. 20 Visualization image of the evaporator with δ=3mm in oscillatory mode

7. Influence of the operating conditions on the performance of the HFMFLHP

The effects of evaporator chamber thickness, filling ratio, and heating power on thermal resistance of the HFMFLHP were examined.

As shown in Fig. 21, thermal resistance depended nonlinearly on evaporator chamber thickness. At FR=30% and Q=30W, δ=3mm presented the highest resistance (1.34K/W), as segmented laminar flow reduced the effective condensation area and film boiling lowered evaporator efficiency. At higher powers (50-70W), stronger vapor-pressure driving and nucleate boiling offset these adverse effects. At FR=50%, resistance followed a hump-shaped trend, peaking at δ=1mm, where film boiling and impeded return flow increased resistance; at δ=2, 3mm, nucleate boiling dominated and resistance decreased. At FR=70%, resistance varied little with thickness because

evaporation and condensation remained matched, except for the oscillatory δ=3mm case. The high charge maintained over 60% of the evaporator wetted and buffered vapor-diffusion fluctuations, limiting relatively low resistance at 70W.



(a) FR=30%

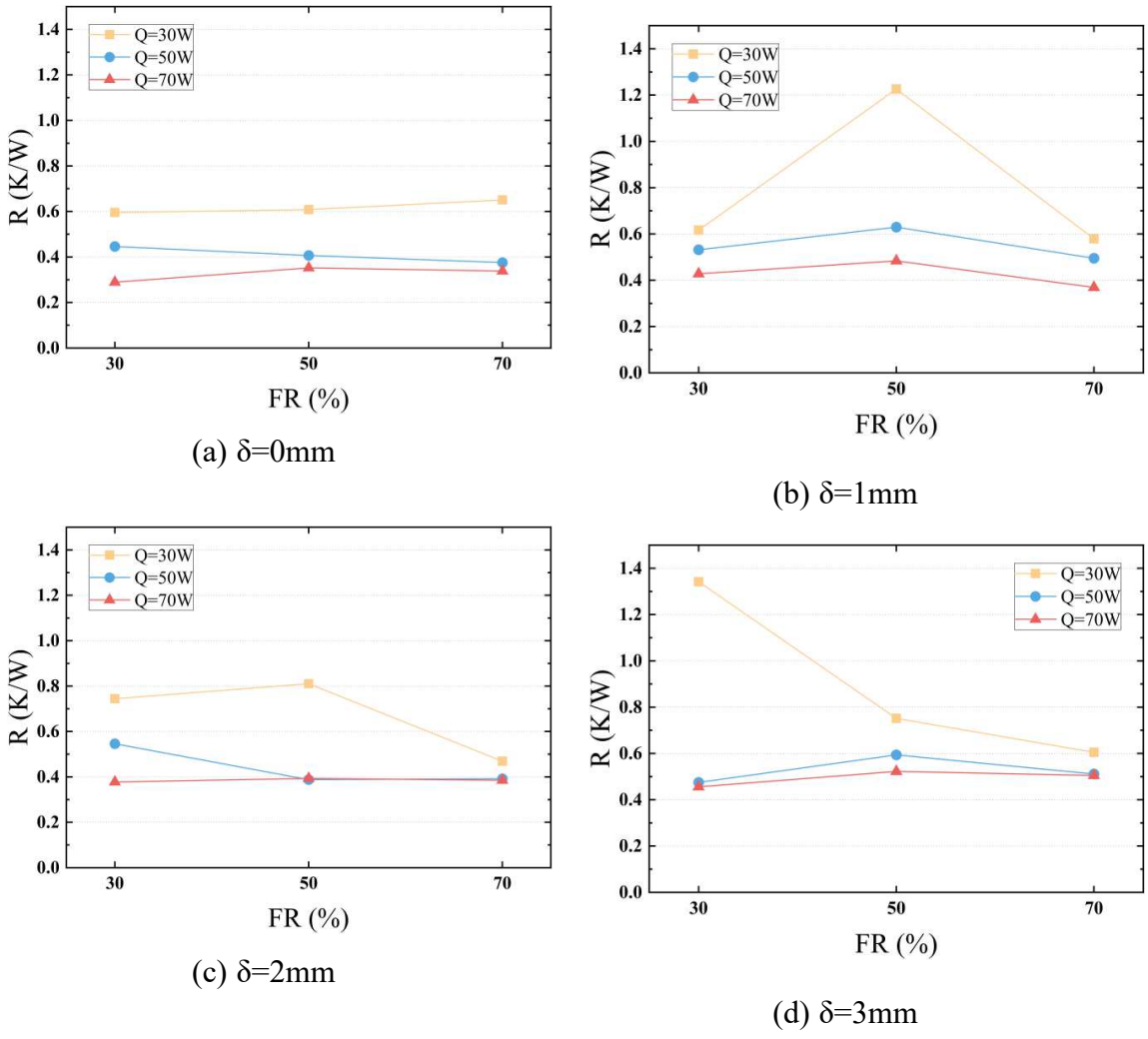
(b) FR=50%

(c) FR=70%

Fig. 21 Influence of the evaporator chamber thickness on the thermal resistance of the HFMFLHP at different filling ratios and heating powers

Thermal resistance of HFMFLHP varied with filling ratio under different evaporator chamber thickness and heating power as in Fig. 22. For δ=0mm (Fig. 22(a)), resistance changed only slightly with filling ratio at all powers, remaining about 0.6, 0.4, and 0.3K/W at 30, 50, and 70W, respectively, because liquid remained present in the evaporator and nucleate boiling dominated despite local dry-out. For δ=1mm (Fig. 22(b)), resistance peaked at FR=50% under all powers, reaching 1.23K/W at 30W,

owing to film-boiling-dominated heat transfer, and oscillatory/transitional operation. For δ=2mm (Fig. 22(c)), at 30W, increasing FR from 50% to 70% reduced resistance by 43% as operation shifted from oscillatory to stable and nucleate boiling became dominant; at 50W, FR=50% gave the best evaporation-condensation balance; at 70W, vapor-pressure-driven circulation weakened the filling-ratio effect. For δ=3mm (Fig. 22(d)), increasing FR from 30% to 50% at 30W reduced resistance by about 44%, from 1.34 to 0.75K/W, as operation shifted from oscillatory to stable, wetted-area fluctuations decreased, and improved liquid-film continuity partially offset the adverse effects of the open chamber.



(a) δ=0mm

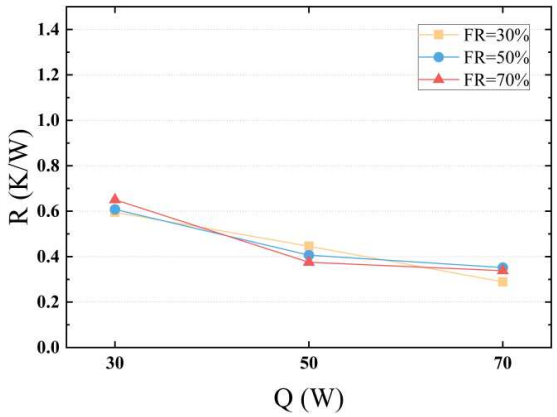
(b) δ=1mm

(c) δ=2mm

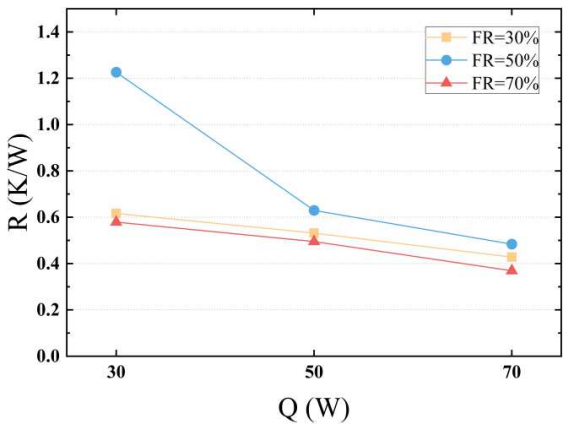
(d) δ=3mm

Fig. 22 Influence of the filling ratio on the thermal resistance of the HFMFLHP at different evaporator chamber thicknesses and heating powers

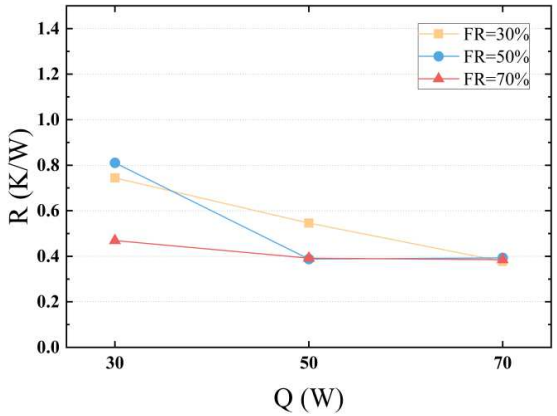
For δ=0mm (Fig. 23(a)), resistance decreased gradually with power at all filling ratios, because capillary-dominated liquid distribution and nucleate boiling persisted in the closed structure. Although wetting-dryout alternation occurred at 70W, optimized condenser flow increased sub-cooled-liquid return and offset instability. For open chamber structures (δ>0mm), resistance became strongly power-dependent at certain filling ratios. At δ=1mm, FR=50%, increasing power from 30 to 50W reduced resistance by 49% (1.23 to 0.63K/W), as higher power enlarged the wetted area and intensified flow disturbances. At δ=2mm, FR=50%, resistance fell sharply to 0.39K/W because nucleate boiling became dominant and condenser resistance decreased. At δ=3mm, FR=30%, resistance dropped 54% (1.34 to 0.62K/W) as nucleate boiling regained dominance. At FR=70%, the higher charge buffered power sensitivity, with only a 12% reduction at δ=3mm. At 30W, open structures generally performed poorly because weak vapor-pressure driving and reduced liquid coverage promoted film boiling and dryout, whereas at Q≥50W, stronger vapor-pressure driving partly offset these effects. Overall, the heating-power effect reflected the balance between vapor-pressure-driven circulation and constraints from chamber structure and filling ratio.



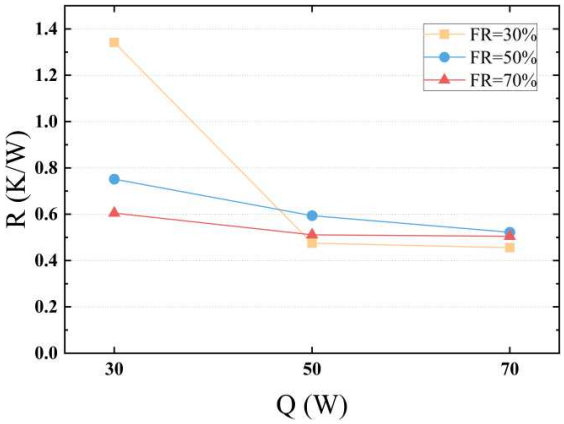
(a) δ=0mm



(b) δ=1mm



(c) δ=2mm



(d) δ=3mm

Fig. 23 Influence of the heating power on the thermal resistance of the HFMFLHP at different evaporator chamber thicknesses and filling ratios

8. Conclusion

In this study, a novel hierarchical fractal micro-grooved flat-plate loop heat pipe (HFMFLHP) was designed and constructed based on the fractal self-similarity rule to address the high-power-density heat dissipation challenges in battery thermal management systems (BTMSs) of new-energy vehicles. By combining visualization experiments with Fourier spectrum analysis, the effects of filling ratio, heating power, and evaporator chamber thickness on the two-phase flow characteristics and heat transfer performance were systematically investigated.

By integrating primary and secondary micro-grooved channels within the evaporator, the heat transfer area within the evaporator of the proposed HFMFLHP was enlarged, and abundant bubble nucleation sites and high-speed vapor escape pathways were provided. The experimental results demonstrated that the proposed structure maintained efficient and stable heat transfer performance in confined spaces. Based on Fourier spectrum analysis, a quantitative classification method for operating modes was established using frequency consistency, amplitude level, and phase deviation as criteria. The 36 experimental conditions were classified into three modes: stable mode, transitional mode, and oscillatory mode based on the three above-mentioned classification criteria. This method effectively identified the system operating states

and provided a quantitative basis for correlating heat transfer performance with two-phase flow stability.

The visualization experiments revealed that a dynamic matching relationship exists among the evaporator chamber thickness, filling ratio, and heating power. The open-chamber thickness must be properly matched with the filling ratio to achieve optimal performance, and an appropriate combination can reduce the thermal resistance through the synergistic effects of vapor-pressure-driven flow and flow-regime optimization. The thermal resistance analysis further indicated that the effect of evaporator chamber thickness on thermal resistance was nonlinear, and that the effects of filling ratio and heating power were strongly coupled with the chamber structure. For open-chamber structures, the thermal resistance became strongly power-dependent at certain filling ratios, whereas a higher filling ratio tended to buffer this sensitivity. The heating-power effect reflected the balance between vapor-pressure-driven circulation and the constraints imposed by chamber structure and filling ratio.

Overall, the proposed optimization strategy provides theoretical support for the design of high-performance flat-plate loop heat pipes and offers valuable insights into efficient and stable thermal management systems for new-energy vehicle batteries and high-power electronic devices.

References

[1] IEA, Global EV Outlook 2023, International Energy Agency, Paris, 2023. https://www.iea.org/reports/global-ev-outlook-2023.

[2] Nitta N, Wu F, Lee J T, et al. Li-ion battery materials: Present and future[J]. Materials today, 2015, 18(5):252-264. DOI:10.1016/j.mattod.2014.10.040

[3] Feng X, Ouyang M, Liu X, et al. Thermal runaway mechanism of lithium ion battery for electric vehicles: A review[J]. Energy storage materials, 2018, 10:246-267. DOI:10.1016/j.ensm.2017.05.013

[4] Rao Z, Wang S. A review of power battery thermal energy management[J]. Renewable and

Sustainable Energy Reviews, 2011, 15(9):4554-4571. DOI:10.1016/j.rser.2011.07.096

[5] Jiang C, Wang J, Yang L, et al. Multi-objective optimization design of a thermal management system for large-capacity energy storage batteries coupling liquid cooling, phase change material and bio-inspired fins [J]. Journal of Energy Storage, 2026, 182:125090. DOI:10.1016/j.est.2026.12509

[6] Sarrafan A, Vafai K. Thermal management of lithium-ion batteries: Air cooling, indirect liquid cooling, and immersion cooling[J]. Advances in Heat Transfer, 2026, in press. DOI: 10.1016/bs.aiht.2026.06.001

[7] Mo C, Tawiah B, Yuen, A, et al. An integrated all-climate battery thermal management system with synergistic functions of preservation, preheating, liquid cooling and thermal runaway mitigation[J]. Energy, 2026, 366: 142651. DOI: 10.1016/j.energy.2026.142651

[8] Gu J, Yang S, Cui W, et al. A novel cylindrical lithium-ion battery thermal management system based on PCM and liquid cooling coupling[J]. Applied Thermal Engineering, 2026, 307:133358. DOI: 10.1016/j.applthermaleng.2026.133358

[9] Yang J, Zhao Y, Diao Y, et al. Experimental study on a thermal management system combining micro heat pipe array with liquid cooling for power lithium-ion batteries[J]. Applied Thermal Engineering, 2026, 303: 132007. DOI: 10.1016/j.applthermaleng.2026.132007

[10] Han C, Yang Y, Wang Z, et al. Study on adaptive modulation of thermal conductivity with temperature for graphite composite films actuated by shape memory alloys[J]. International Journal of Heat and Mass Transfer, 2025, 253:127533. DOI: 10.1016/j.ijheatmasstransfer.2025.127533

[11] Han C, Cheng Y, Wang Z, Zheng Y. A study on the cooling characteristics of radiator for battery hot spots based on temperature hydrogel adaptive valve[J]. Journal of Energy Storage, 2024, 102:114107. DOI: 10.1016/j.est.2024.114107

[12] Kumar M, Khan S Y, Liu S, et al. Scientific mapping and review of the research landscape in battery thermal management strategies using heat pipe[J]. Journal of Energy Storage, 2024, 103. DOI: 10.1016/j.est.2024.114147

[13] Huang Y, Si L, Xu C, et al. Simulation study on heat transfer and flow performance of pump-driven microchannel-separated heat pipe system[J]. Energies, 2025, 18: 5882. DOI: 10.3390/en18225882

[14] Hadi H, Imani A, Islami S, et al. Geometric optimization of inter-cell spacing for enhanced phase-change cooling in a dual-evaporator loop heat pipe battery thermal management system[J].

Energy Conversion and Management: X, 2026, 31:102144. DOI: 10.1016/j.ecmx.2026.102144

[15] Sahoo R. Thermo-hydraulic characteristics of radiator with various shape nanoparticle-based ternary hybrid nanofluid[J]. Powder Technology, 2020, 370: 19-28. DOI: 10.1016/j.powtec.2020.05.013

[16] Nomura R, Hashimoto M, Alasli A, et al. Thermal performance evaluation of a parylene-coated polydimethylsiloxane loop heat pipe featuring a micropillar evaporator[J]. Applied Thermal Engineering, 2025, 272:126249. DOI: 10.1016/j.applthermaleng.2025.126249

[17] Wang X, Zhai M, Teng S, et al. Thermal performance enhancement and flow optimization of an interconnected microchannel loop heat pipe for battery cooling [J]. Applied Thermal Engineering, 2026, 300:131597. DOI: 10.1016/j.applthermaleng.2026.131597

[18] Ling L, Xia Y, Zhao L, et al. Experimental investigation on the thermal performance of a novel loop heat pipe (LHP) with micro-channel structure[J]. Applied Thermal Engineering, 2024, 238:122046. DOI:10.1016/j.applthermaleng.2023.122046

[19] Tharayil T, Asirvatham L G, Ravindran V, et al. Effect of filling ratio on the performance of a novel miniature loop heat pipe having different diameter transport lines[J]. Applied Thermal Engineering, 2016, 106:588-600. DOI: 10.1016/j.applthermaleng.2016.05.125

[20] Del Col D, Bortolin S, Cavallini A, et al. Effect of cross sectional shape during condensation in a single square minichannel[J]. International Journal of Heat and Mass Transfer, 2011, 54(17):3909-3920. DOI:10.1016/j.ijheatmasstransfer.2011.04.035

[21] Wang D, Wang J, Bao X, et al. Experimental study on hydraulic and thermal characteristics of composite porous wick with spherical–dendritic powders[J]. Journal of Thermal Analysis and Calorimetry, 2020, 141(1):107-117. DOI:10.1007/s10973-019-08920-3

[22] Hong S, Zhang X, Tang Y, et al. Experiment research on the effect of the evaporator's configuration design of an innovative ultra-thin looped heat pipe[J]. International Journal of Heat and Mass Transfer, 2016, 92:497-506. DOI:10.1016/j.ijheatmasstransfer.2015.08.070

[23] Cao B, Li J, Wu Z, et al. Flow boiling in novel radial microchannels for cooling of electronic devices and modules of annular temperature distribution[J]. International Journal of Heat and Mass Transfer, 2025, 239:126555. DOI:10.1016/j.ijheatmasstransfer.2024.126555

[24] Thackeray M, Thomas J, Whittingham M. Science and Applications of Mixed Conductors for Lithium Batteries[J]. MRS Bulletin, 2000, 25(3):39-46. DOI:10.1557/mrs2000.17

[25] Chernysheva M, Vershinin S, Maydanik Y. Development and investigation of a loop heat pipe at a high concentration of heat load[J]. International Journal of Heat and Mass Transfer, 2022, 197:123316. DOI:10.1016/j.ijheatmasstransfer.2022.123316

[26] Tian W, He S, Liu Z, et al. Experimental investigation of a miniature loop heat pipe with eccentric evaporator for cooling electronics[J]. Applied Thermal Engineering, 2019, 159:113982. DOI:10.1016/j.applthermaleng.2019.113982

[27] Falk RS, Nussbaum RD. A new approach to numerical computation of Hausdorff Dimension of iterated function systems: Applications to complex continued fractions[J]. Integral Equations and Operator Theory, 2018, 90: 61. DOI:10.1007/s00020-018-2485-z

[28] Ma DF, Wang GW, Ma YG, et al. Hydrodynamics behavior and mass transfer performance of gas-liquid two-phase flow in the honeycomb fractal microreactor[J]. Chemical Engineering Journal, 2023, 462:142228. DOI:10.1016/j.cej.2023.142228

[29] Yu M, Zhu XL, Li MJ, et al. Impact of working fluid filling ratio on the performance of a micro-channel loop heat pipe based solar PV/T heat and power system [J]. Energy, 2025, 317: 134716. DOI:10.1016/j.energy.2025.134716

[30] Park S H. Energy dissipation rate and pressure fluctuations in a three phase fluidized bed with a large column diameter[J]. Korean Journal of Chemical Engineering, 2004, 21:1066-1071. DOI:10.1007/BF02705594